

# High-Frequency GaAs Optomechanical Bullseye Resonator

N. C. Carvalho,<sup>1,\*</sup> R. Benevides,<sup>1</sup> M. Ménard,<sup>2</sup> G. S. Wiederhecker,<sup>1</sup> N. C. Frateschi,<sup>1</sup> and T. P. M. Alegre<sup>1,†</sup>

<sup>1</sup>*Applied Physics Department and Photonics Research Center, University of Campinas, Campinas, SP, Brazil*

<sup>2</sup>*Department of Computer Science, Université du Québec à Montréal, Montréal, Canada*

The integration of optomechanics and optoelectronics in a single device opens new possibilities for developing information technology and exploring fundamental phenomena. Gallium arsenide is a well-known material that can bridge the gap between the functionalities of optomechanical devices and optical gain media. Here, we experimentally demonstrate a high-frequency GaAs optomechanical resonator with a ring-type bullseye geometry that is unprecedented in this platform. We measured mechanical modes up to 3.4GHz with quality factors of 4000 (at 77K) and reached optomechanical coupling rates up to 39kHz at telecom wavelengths. The temperature dependence of mechanical losses was assessed and demonstrate the efficiency and anisotropy resilience of the bullseye anchor loss suppression. Such characteristics are valuable for active optomechanics, coherent microwave-to-optics conversion via piezo-mechanics and other implementations of high-frequency oscillators in III-V materials.

## INTRODUCTION

The engineering of light-matter interaction in optomechanical devices has allowed the observation of very relevant fundamental phenomena such as gravitational waves [1] and ground-state cooling [2]; and consequently has enabled important developments in information science technology [3, 4]. For the past decade, silicon has been the material of choice for most on-chip optomechanics experiments. However, as we move towards high power efficiency and quantum-level control, device design becomes more challenging and material properties more restrictive, which have driven intense research into alternative materials [5–8]. Therefore, gallium arsenide (GaAs) arises as a mature platform with potential to pair up or overcome silicon in many properties, such as light confinement and optomechanical coupling strength, due to its high-refractive index and large photo-elastic coefficients [9]. Moreover, the optical losses that often impair the performance of GaAs have been mitigated by improved etching and surface passivation techniques, leading to optical quality factors of over a million [10].

Developing optomechanical resonators based on III-V materials would not only enable their disruptive integration with coherent light sources and single quantum emitters, but also open routes to explore the interplay of gain and loss in non-Hermitian physical systems [11]. Besides its advantageous optoelectronic properties, GaAs also offers other convenient characteristics, such as piezoelectricity, revealing its suitability for wavelength conversion mediated by piezo-optomechanics [12], enabling thus the ultimate integration and control of charge carriers, light, sound, and microwave fields.

To unleash such outstanding properties of GaAs and enable an optomechanical device operation in the resolved-sideband regime, a design supporting high mechanical frequencies must be devised beyond simple microdisks [13], but more practical than complex optomechanical crystals [9]. Despite recent

efforts with nanobeam cavities with impressive optomechanical coupling rates, mechanical frequencies have not exceeded 2.8GHz in GaAs [14, 15]. In this work, we demonstrate GaAs optomechanical devices built using a bullseye design that allows for very high mechanical quality factors and measured mechanical modes up to 3.4GHz, with potential to explore even higher frequency modes, according to our simulations. This unconventional geometry, originally devised by Santos *et al.* [16] using silicon, consists of a ring-type cavity resonator obtained by patterning a nano-structured circular grating over a micro-disk, as shown in the diagram in Fig. 1 (a1). In this design, the mechanical waves are confined to the outermost ring using a radial phononic shield, which also isolates the ring cavity from the supporting pedestal, inhibiting anchor losses.

A key advantage of the bullseye design, compared to nanobeams or optomechanical crystal devices, is the complete decoupling between optical and mechanical resonance frequencies. The former is mostly influenced by the radius of the disk,  $R$  in Fig. 1 (a1), whereas the latter will be defined by the external ring width ( $w_{\text{ring}}$ ). In this way, mechanical frequencies can be increased by narrowing down the external ring, with minimal impact on the optical frequencies, as long as  $w_{\text{ring}} \gtrsim 500 \mu\text{m}$  [16]. The other critical free dimensions are  $a$ ,  $w$  and  $t$ , that can be adjusted to create a phononic bandgap that fits the mechanical ring modes.

## DESIGN AND FABRICATION

Our GaAs bullseye design is based on a nominal geometry with a disk with radius of  $6 \mu\text{m}$  and grating dimensions set to  $a = 600 \text{nm}$ ,  $w = 120 \text{nm}$  and  $t = 50 \text{nm}$ , as shown in Fig. 1 (a1). This grating is designed using a 2D cartesian Finite Element Method (FEM) model of a linear crystal to approximate the actual circular grating. Regardless of the curvature of the radial shield, it created a partial phononic bandgap that resulted in a mechanical frequency stopband in the range between  $\sim 3 \text{GHz}$  and  $4 \text{GHz}$ , as shown in the band-diagram of Fig. 1 (b). The optomechanical coupling rate,  $g_0/(2\pi)$ , for the full bullseye structure is shown in Fig. 1 (c). Our simulations show that three mechanical modes couple to the optical field, as highlighted by the gray dashed lines between 2

\* natccar@ifi.unicamp.br

† alegre@unicamp.br

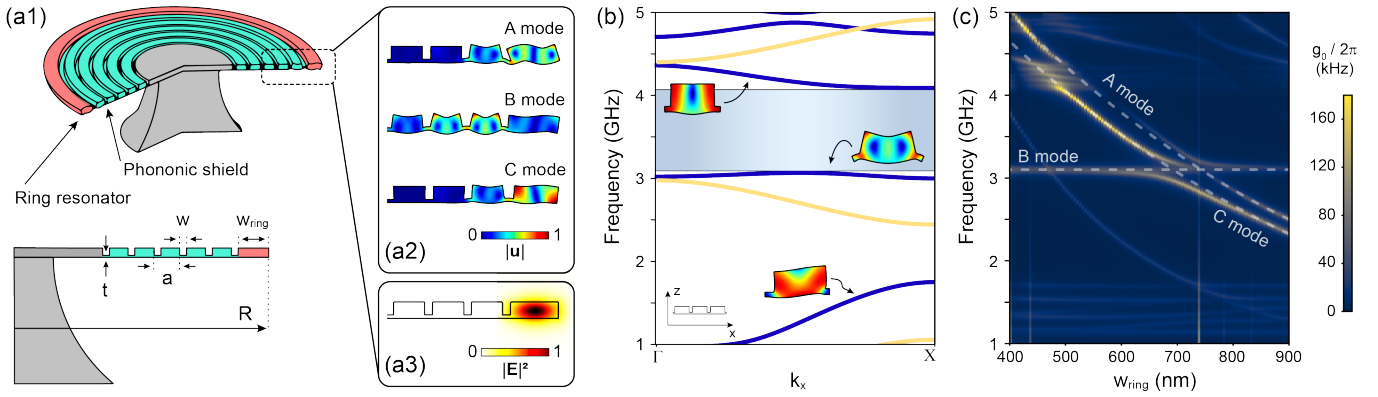


FIG. 1. (a1) Illustration of the bullseye resonator (top) and geometric parameters (bottom). Inset: (a2) simulated displacement profile of the mechanical modes and (a3) electric amplitude of the whispering gallery optical mode with transverse electric polarization (bottom). (b) The blue (yellow) lines are the mechanical bands of the bullseye grating simulated as a linear crystal for  $x$ -polarized or  $z$ -polarized ( $y$ -polarized) modes. The shaded blue is the target bandgap and the insets show the mechanical deformation for the modes at the band-edge ( $X$ -point). (c) 2D simulation results of the optomechanical coupling rate ( $g_0/(2\pi)$ ), the gray dashed lines are drawn as a guide to the eyes. The grading parameters in (b) and (c) are  $a = 600$  nm,  $w = 120$  nm and  $t = 50$  nm.

and 5 GHz. The mechanical displacement profiles of these modes are shown in Fig. 1 (a2), followed by the first radial-order transverse electric (TE) optical mode to which they are coupled (in Fig. 1 (a3)). It reveals that C is the desired ring-type breathing mode, while A is a flexural ring mode and B is a grating mode that is almost independent of the external ring size.

The devices were fabricated from a GaAs/Al<sub>0.7</sub>Ga<sub>0.3</sub>As stack (250 nm/2000 nm), that was grown over a GaAs substrate using molecular beam epitaxy (Canadian Photonics Fabrication Centre). Differently from the previous silicon bullseye, the GaAs structure was defined using electron beam lithography [17]. The fabrication steps of the GaAs bullseye samples are summarized in Fig. 2 (a). The devices were patterned on the top of the GaAs wafer through a single plasma etching step. We used positive electro-resist (ZEP-520A) and managed to define grating grooves and remove all the material outside the microdisk region using the aspect-ratio dependent etching, where the etching rate of narrower gaps is lower in comparison to wider regions (Fig. 2 (a) - inset). The bullseye disks were then released from the substrate by a selective wet etching of buffer the AlGaAs layer with hydrofluoric acid (HF), followed by standard organic cleaning. This advantageous technique relieved the necessity of multiple lithography process that would introduce complex alignment procedures.

Figures 2 (b) and (c) have scanning microscope images of exemplar samples. The former shows the final device surrounded by the *parking lot*, which was designed to support the fiber loop. Top view images, such as in Fig. 2 (c), were used to characterize the dimensions of the devices. The disk radius ( $R$ ),  $w_{\text{ring}}$ ,  $a$  and  $w$  were measured through this method, whereas  $t$  was only estimated from the etching rate, which was calibrated prior to the fabrication of the devices. Electron beam proximity effects caused the first outer groove ( $w_1$ ) to have a narrower width in comparison to the inner grooves ( $w$ ). As detailed in the Supplementary Material, both  $w_1$  and  $t$  were

found by matching the measured and simulated values for the optical mode dispersion of our device. All those geometrical values were then used in the FEM simulations of Fig. 3.

## RESULTS AND DISCUSSION

The optomechanical properties of the resonators were characterized in the setup schematically represented in Fig. 3 (a). The bullseye microcavity was probed via evanescent coupling with a tapered fiber loop continuously fed by a tunable C-band laser (New Focus TLB-6728). The transmitted optical signal was then split and simultaneously measured by a slow and a fast detector. The DC component gave information about the optical response of the cavity, while the fast signal was measured by an electrical spectrum analyzer that read out the mechanical mode signatures imparted on the transmitted optical signal.

We experimentally investigated two devices with different  $w_{\text{ring}}$  sizes: 700 nm and 740 nm, at room temperature and atmospheric pressure. The optical spectrum of the 740 nm sample is displayed in Fig. 3 (b). The inset has a mode doublet (counter-propagating whispering-gallery-modes) presenting total linewidths,  $\kappa/(2\pi)$ , of  $\sim 6$  GHz (Q-factor  $\sim 3 \times 10^4$ ), which was a typical value measured in our samples. These modes provided the strongest readout of the mechanical modes and were identified as the second-radial order modes with quasi-TE polarization (major component along the radial direction). The identification was based on the comparison between the measured and simulated frequency dependence of the free spectral range (due to group velocity dispersion) [18] - see Supplementary Material for details. Although, larger  $g_0$  is predicted for optomechanical coupling through the first radial order mode, our measurement scheme was sensitive to  $g_0^2/\kappa$  and, therefore, the detection of the mechanical interaction with such optical modes was compromised by their larger

linewidths.

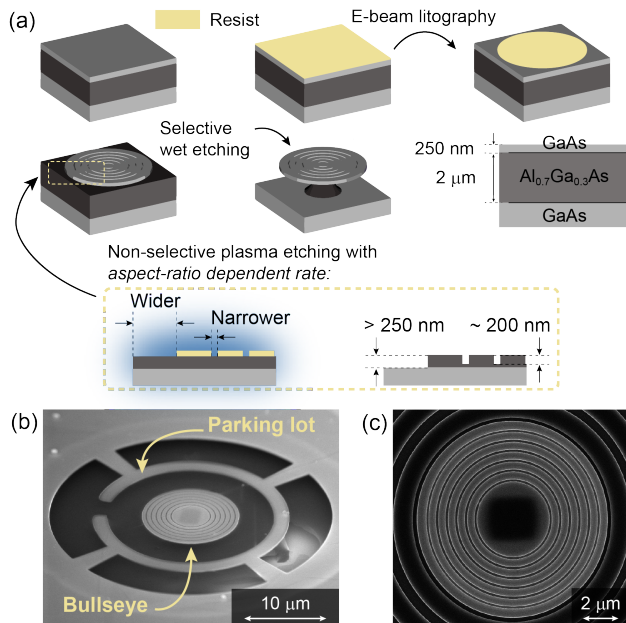


FIG. 2. (a) Simplified illustration of the bullseye fabrication steps. The inset contains a diagram that highlights the plasma etching rate contrast for regions of different sizes. (b) Scanning electron microscope image of a typical device (bullseye resonator surrounded by the *parking lot*, a structure designed to stabilize the tapered fiber loop). (c) Top view of a sample.

A 3.29 GHz mechanical resonance is measured in the 740 nm  $w_{\text{ring}}$  and shown in Fig. 3 (c). The Lorentzian fit determined a mechanical quality factor ( $Q_m$ ) of 900 and the calibration of  $g_0$  – through the comparison between the phase modulator RF-tone and the optical transduction of the cavity [19] – results in an optomechanical coupling rate of  $g_0/(2\pi) = 34$  kHz. Analogously, we obtained a  $Q_m$  of 1200 and a  $g_0/(2\pi) = 39$  kHz for a 3.13 GHz mode of the 700 nm  $w_{\text{ring}}$  sample. The numerical simulations and a broad experimental mechanical spectrum up to  $\sim 3.4$  GHz for the 740 nm  $w_{\text{ring}}$  are shown in Fig. 3 (d1)-(d4).

The multiple peaks observed in the experimental spectra of Fig. 3 (d4) are not consistent with axisymmetric simulations that predict a single peak for each mechanical mode (A, B and C in Fig. 1 (a1)). Therefore, we employed a three-dimensional FEM model to account for the well-known elastic anisotropy of GaAs and precisely identify the mechanical modes. Indeed, as the material anisotropy is gradually increased in the 3D simulations, a clear degeneracy lifting of the mechanical mode frequencies is observed, as shown in Fig. 4 (d1)-(d3) by sweeping the anisotropy parameter  $\eta$ . Here,  $\eta = 0$  corresponds to an isotropic device and  $\eta = 1$  is the full anisotropic case, according to the relation  $c_{44}^*(\eta) = \eta c_{44} + (1 - \eta)(c_{11} + c_{22})/2$  for the GaAs stiffness tensor component.

The isotropic mechanical displacement profile shown in Fig. 3 (d5) ( $\eta = 0$ ) corresponds to the prominent peak in Fig. 3 (d1). It demonstrates that only the C-mode has rele-

vant optomechanical coupling rate to the second-radial order optical mode (see Supplementary Material). Moreover, despite the modification of the mode structure after the material loss of symmetry, the measured mechanical mode, highlighted in shaded gray in Fig. 3 (d3)-(d4), still can be related to the C-mode (external ring breathing mode) as can be seen in Fig. 3 (d5) ( $\eta = 1$ ). The 3D modeling also shows that the mechanical grating isolation is resilient to the anisotropy and predicts a reduced  $g_0$  to the second-radial order optical mode when comparing to Fig. 1 (c). Both information agrees quite reasonably well with the calibrated data presented in Fig. 3 (c).

In order to investigate the role of the mechanical grating in inhibiting clamping losses, thermal channels of dissipation had to be suppressed. Therefore, our samples were cooled down to the temperature of liquid nitrogen. Figure 4 (a1) contains the measured mechanical C-mode of the 700 nm  $w_{\text{ring}}$ . At the temperature of  $\sim 80$  K, a  $Q_m$  of  $4 \times 10^3$  was measured, an improvement over three times in comparison to room temperature data. To observe the behavior of the mechanical linewidth ( $\Gamma_m$ ) as a function of the cavity input power, we performed a laser power sweep - frequency tuned for maximum optomechanical transduction, on the blue side of the optical resonance. As the power was increased, we noticed a simultaneously increase in the mechanical linewidth and a red-shift,  $\Delta f = f - f_0$ , where  $f_0$  is the initial mechanical mode frequency and  $f$  is its frequency at a given optical input power, as shown in Fig. 4 (a2).

In Fig. 4 (b) we show that  $\Delta f$  goes down a few MHz when approaching 1 mW of optical input power. This effect is explained by the cavity heating, that causes the material to expand, modifying the mode frequency [20]. We calculated this shift and plotted against the data by assuming that at very low power this heating was negligible, i. e.,  $\Delta f = 0$ , and the initial reading of the temperature sensor was a good approximation for the cavity temperature. Then, it was possible to estimate a linear relation between temperature and the input power to the resonator, which was done by comparing the measured power induced frequency shift to the expected shift caused by thermal expansion.

We also measured the decrease of  $Q_m$  with power, as displayed in Fig. 4 (c), that contains the data of Fig. 4 (a1) and (a2) in the extreme input power values, highlighted in light blue (low power) and light red (high power), respectively. In order to understand this behavior, we included other losses mechanism to the mechanical linewidth. When neglecting anchor losses, the mechanical linewidth broadening of nanomechanical resonators are then in general dominated by phonon-phonon interactions and scattering by defects. The former can introduce losses via relaxation of thermal phonons, whereas the second dissipates mechanical energy by coupling strain waves to two-level systems (TLS) [21, 22].

To estimate the linewidth of our sample, we calculated the anharmonic and the TLS mechanical attenuation through the methods described in Ref. [23], with material constants found in Refs. [24–27]. From 300 K to 80 K, our bullseye resonators falls into the Akhiezer regime [28],  $\omega_m \tau_{ph} \lesssim 1$ , where  $\tau_{ph}$  is the phonon relaxation time for this channel and  $\omega_m$  is the me-

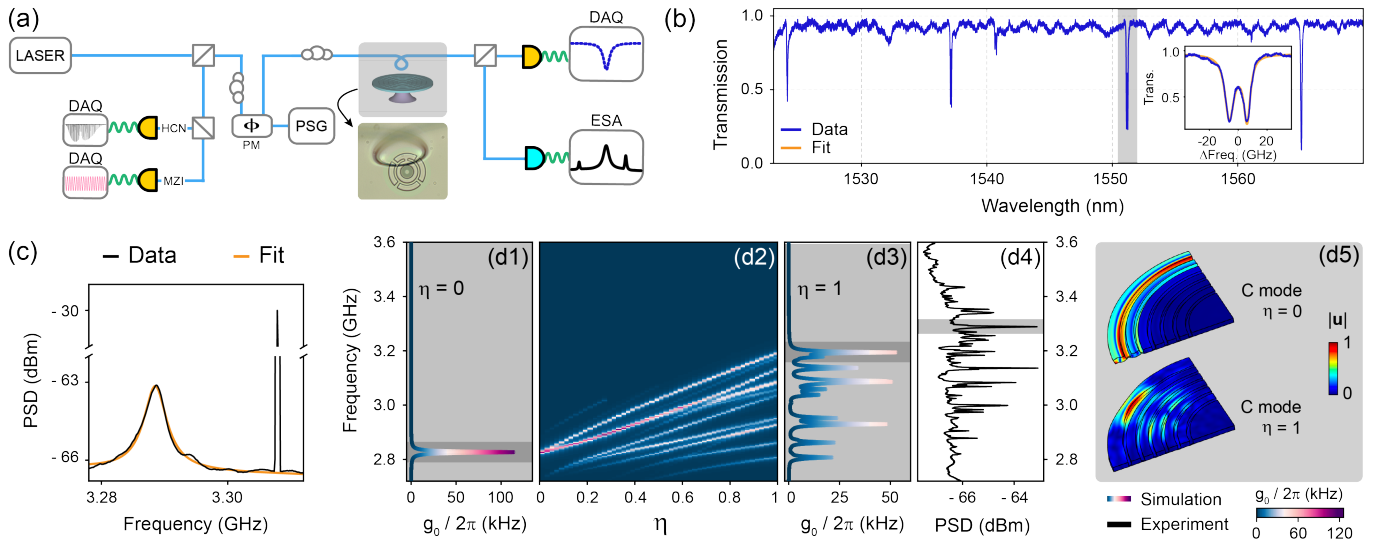


FIG. 3. (a) Optomechanical characterization setup (DAQ - Data Acquisition System, PSG - Power Signal Generator, ESA - Electrical Spectrum Analyzer, PM - Phase Modulator, HCN - Hydrogen Cyanide wavelength reference and MZI - Mach-Zehnder Interferometer). Inset: optical microscope image of the tapered fiber loop coupled to a device. (b) Optical transmission spectrum of the  $w_{\text{ring}} = 740\text{ nm}$  sample. The inset shows the optical modes highlighted in light gray. The orange line is the Lorentzian fit. (c) Power spectral density (PSD) of selected mechanical mode of the  $740\text{ nm}$  sample (highlighted in shaded gray in (d4)) with respective  $g_0$  calibration peak (the orange line is the Lorentzian fit). 3D FEM simulations of: (d1) the mechanical spectra when  $\eta = 0$  (fully isotropic), (d2) the optomechanical coupling rate as a function of the material anisotropy parameter ( $\eta$ ) and (d3) mechanical spectra when  $\eta = 1$  (fully anisotropic). (d4) Experimental PSD of the mechanical modes. (d5) Simulated mechanical displacement profiles highlighted in light gray in (d1) and (d3). The information in (d1)-(d5) corresponds to the  $w_{\text{ring}} = 740\text{ nm}$  and all experimental data was acquired at room temperature and atmospheric pressure.

chanical resonator angular frequency. Thermoelastic losses obtained from FEM was found to be several orders of magnitude lower than the Akhiezer damping and are neglected in this analysis. The double-well potentials parameters of our TLS dissipation model were obtained from Ref. [29], where GaAs microdisks were investigated; as such values are highly material dependent and must not suffer significant changes between the slightly different geometries, they serve as a reasonable approximation for our devices.

Our model results are displayed in Fig. 4 (d), where the inset has a direct comparison of the measured mechanical quality factors (3.1 GHz mode) to the theory. Furthermore the measurement of  $Q_m$  as the input laser power was increased, gives a hint about the accuracy of our mechanical dissipation model, that correctly predicts the  $Q_m$  optical power dependence, as shown in Fig. 4 (c). The total model not only accounted for the thermal sources of mechanical dissipation (Akhiezer and TLS), but also included the linewidth modification expected from optomechanical backaction. If the measured  $Q_m$  was dominated by optomechanical dynamics, an opposite trend should be observed, with increasing (decreasing) Q-factor ( $\Gamma_m$ ) for higher input power. Therefore, we can see that optomechanical anti-damping is not playing a significant role in the mechanical linewidth, indicating that it is dominated by temperature dependent dissipation. Moreover, the 3D calculation including mechanical clamping and perfectly matched layers predicted mechanical Q-factors between  $10^4 - 10^7$  for the ring modes (Fig. 3 (d4)), which are at least one order of magnitude higher than the measured values,

thus suggesting that our device is not limited by anchor losses.

## CONCLUSION

In summary, we designed a GaAs bullseye resonator with a phononic grating operating between 3 GHz and 4 GHz. The fabricated devices show modes ranging in  $\sim 3.0\text{ GHz} - 3.4\text{ GHz}$  with optomechanical coupling rates of up to 39 kHz and mechanical quality factor of 4000 when cooled down to the liquid nitrogen temperature. In order to harness the full potential of the GaAs bullseye resonators, the regime of high optomechanical cooperativity must be accessible and, thus, higher optical and mechanical Q-factors must be achieved. The former could be obtained by minimizing surface absorption [10] and roughness [17] with alumina passivation and electroresist thermal reflow. Additionally, mechanical dissipation is expected to be drastically reduced at lower temperatures as thermal anharmonic losses are reduced. Incorporating III-V quantum emitters to the bullseye cavity would also enable the study of active optomechanics, opening a plethora of possibilities, including the creation of an alternative approach for hybrid systems that couples single emitters to mechanical strain [30] and the realization of a mechanically modulated light sources [31]. Microwave-to-optical conversion, on the other hand, could take advantage of higher mechanical frequencies enabled by narrower  $w_{\text{ring}}$ 's or exploring higher order mechanical modes. Finally, the bullseye design was shown to be robust across different material platforms

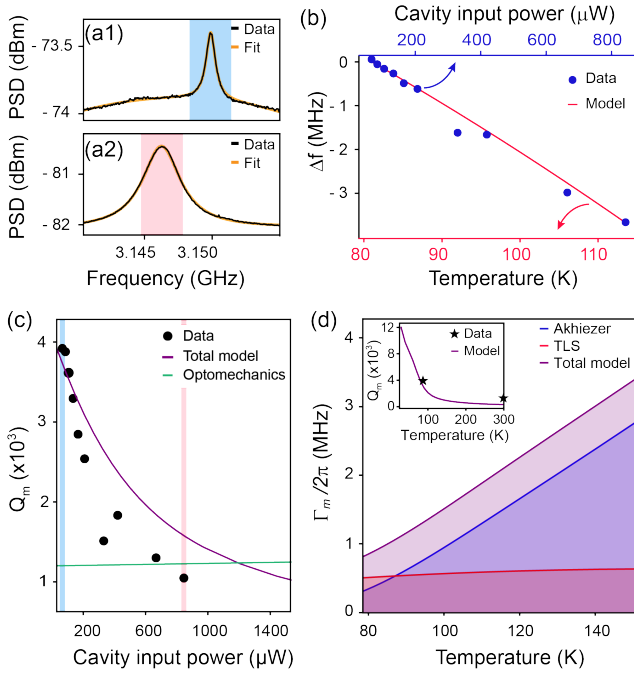


FIG. 4. Temperature dependence of the 3.1 GHz mode of the 700 nm ring width sample: PSD of the mechanical resonance measured for the lower (light blue - (a1)) and higher (light red - (a2)) cavity input power (Lorentzian fits in orange); (b) measured mechanical frequency shift ( $\Delta f$ ) as a function of the cavity power (blue) and computed frequency shift resulting from the  $w_{\text{ring}}$  thermal expansion as a function of temperature (red); (c) comparison of the experimental mechanical Q-factor ( $Q_m$ ) power dependence to the total model of  $Q_m$  (Akhiezer, TLS and optomechanical anti-damping) and the calculated optomechanical backaction effect only (narrowing of the mechanical linewidth with increasing power) - light blue and red strips correspond to the data of the resonant modes shown in (a1) and (a2), respectively; (d) nanomechanical dissipation model of the bullseye resonator. Inset: calculated  $Q_m$  compared to the experimental data of low and room temperature measurements.

and could be extended to other semiconductor materials with lower non-linear optical losses, such as GaP [32, 33].

## ACKNOWLEDGMENTS

The authors would like to acknowledge CCSNano-UNICAMP for providing the micro-fabrication infrastructure and CMC Microsystems for providing access to MBE epitaxy and the GaAs wafers. This work was supported by São Paulo Research Foundation (FAPESP) through grants 2017/19770-1, 2016/18308-0, 2018/15580-6, 2018/15577-5, 2018/25339-4, Coordenação de Aperfeiçoamento de Pessoal de Nível Superior - Brasil (CAPES) (Finance Code 001), Financiadora de Estudos e Projetos and the National Sciences and Engineering Research Council (NSERC) of Canada.

## SUPPLEMENTARY MATERIAL

See Supplementary Material for details on the characterization of the optical modes through the frequency dependence of the free spectral range.

## DATA AVAILABILITY

The data that support the findings of this study are available from the corresponding author upon reasonable request.

- [1] B. P. Abbott, R. Abbott, T. D. Abbott, M. R. Abernathy, F. Acernese, K. Ackley, C. Adams, T. Adams, P. Addesso, R. X. Adhikari, *et al.*, *Physical Review Letters* **116**, 061102 (2016).
- [2] J. Chan, T. P. Alegre, A. H. Safavi-Naeini, J. T. Hill, A. Krause, S. Gröblacher, M. Aspelmeyer, and O. Painter, *Nature* **478**, 89 (2011), arXiv:1106.3614.
- [3] J. T. Hill, A. H. Safavi-Naeini, J. Chan, and O. Painter, *Nature Communications* **3** (2012), 10.1038/ncomms2201, arXiv:1206.0704.
- [4] A. D. O’Connell, M. Hofheinz, M. Ansmann, R. C. Bialczak, M. Lenander, E. Lucero, M. Neeley, D. Sank, H. Wang, M. Weides, J. Wenner, J. M. Martinis, and A. N. Cleland, *Nature* **464**, 697 (2010).
- [5] B. Guha, S. Mariani, A. Lemaître, S. Combrié, G. Leo, and I. Favero, *Optics Express* **25**, 24639 (2017), arXiv:1710.00632.
- [6] K. M. Morozov, K. A. Ivanov, E. I. Girshova, A. S. Sokolovskii, and A. P. Mikitchuk, in *Journal of Physics: Conference Series*, Vol. 1410 (IOP Publishing, 2019) p. 012156.
- [7] C. L. Zou, X. Han, L. Jiang, and H. X. Tang, *Physical Review A* **94**, 13812 (2016), arXiv:1604.06027.
- [8] M. Mitchell, D. P. Lake, and P. E. Barclay, *APL Photonics* **4**, 016101 (2019).
- [9] K. C. Balram, M. Davanço, J. Y. Lim, J. D. Song, and K. Srinivasan, *Optica* **1**, 414 (2014), arXiv:1409.6198.
- [10] B. Guha, F. Marsault, F. Cadiz, L. Morgenroth, V. Ulin, V. Berkovitz, A. Lemaître, C. Gomez, A. Amo, S. Combrié, B. Gérard, G. Leo, and I. Favero, *Optica* **4**, 218 (2017).
- [11] K. Özdemir, S. Rotter, F. Nori, and L. Yang, “Parity–time symmetry and exceptional points in photonics,” (2019).
- [12] M. Wu, E. Zeuthen, K. C. Balram, and K. Srinivasan, *Physical Review Applied* **13** (2020), 10.1103/PhysRevApplied.13.014027, arXiv:1907.04830.
- [13] C. Baker, W. Hease, D.-T. Nguyen, A. Andronico, S. Ducci, G. Leo, and I. Favero, *Optics Express* **22**, 14072 (2014), arXiv:1403.4269.
- [14] K. C. Balram, M. I. Davanço, J. D. Song, and K. Srinivasan, *Nature Photonics* **10**, 346 (2016), arXiv:1508.01486.

- [15] M. Forsch, R. Stockill, A. Wallucks, I. Marinković, C. Gärtner, R. A. Norte, F. van Otten, A. Fiore, K. Srinivasan, and S. Gröblacher, *Nature Physics* **16**, 69 (2020), arXiv:1812.07588.
- [16] F. G. S. Santos, Y. A. V. Espinel, G. O. Luiz, R. S. Benevides, G. S. Wiederhecker, and T. P. Mayer Alegre, *Optics Express* **25**, 508 (2017), arXiv:1605.06318.
- [17] R. Benevides, M. Ménard, G. S. Wiederhecker, and T. P. Mayer Alegre, *Optical Materials Express* **10**, 57 (2020), arXiv:1909.06881.
- [18] L. Fujii, M. Inga, J. H. Soares, Y. A. V. Espinel, T. P. Mayer Alegre, and G. S. Wiederhecker, *Optics Letters* **45**, 3232 (2020), arXiv:2003.11625.
- [19] M. L. Gorodetsky, A. Schliesser, G. Anetsberger, S. Deleglise, and T. J. Kippenberg, *Optics Express* **18**, 23236 (2010).
- [20] R. Benevides, N. C. Carvalho, M. Ménard, N. C. Frateschi, G. S. Wiederhecker, and T. P. Alegre, in *Optics InfoBase Conference Papers*, Vol. Part F123- (Optical Society of America, 2018) pp. W4D–4.
- [21] P. Mohanty, D. A. Harrington, K. L. Ekinci, Y. T. Yang, M. J. Murphy, and M. L. Roukes, *Physical Review B - Condensed Matter and Materials Physics* **66**, 854161 (2002).
- [22] W. A. Phillips, *Reports on Progress in Physics* **50**, 1657 (1987).
- [23] R. Vacher, E. Courtens, and M. Foret, *Physical Review B* **72**, 214205 (2005), arXiv:0505560 [cond-mat].
- [24] J. S. Blakemore, *Journal of Applied Physics* **53**, R123 (1982).
- [25] R. I. Cottam and G. A. Saunders, *Journal of Physics C: Solid State Physics* **7**, 2447 (1974).
- [26] R. Nava and J. Romero, *The Journal of the Acoustical Society of America* **64**, 529 (1978).
- [27] R. I. Cottam and G. A. Saunders, *Journal of Physics C: Solid State Physics* **6**, 2105 (1973).
- [28] T. P. M. Alegre, A. Safavi-Naeini, M. Winger, and O. Painter, *Optics Express* **19**, 5658 (2011), arXiv:1012.2556.
- [29] M. Hamoumi, P. E. Allain, W. Hease, E. Gil-Santos, L. Morgenroth, B. Gérard, A. Lemaître, G. Leo, and I. Favero, *Physical Review Letters* **120** (2018), 10.1103/PhysRevLett.120.223601, arXiv:1801.09078.
- [30] I. Yeo, P. L. De Assis, A. Gloppe, E. Dupont-Ferrier, P. Verlot, N. S. Malik, E. Dupuy, J. Claudon, J. M. Gérard, A. Auffèves, G. Nogues, S. Seidelin, J. P. Poizat, O. Arcizet, and M. Richard, *Nature Nanotechnology* **9**, 106 (2014), arXiv:1306.4209.
- [31] D. Princepe, G. S. Wiederhecker, I. Favero, and N. C. Frateschi, *IEEE Photonics Journal* **10**, 1 (2018).
- [32] I. Ghorbel, F. Swiadek, R. Zhu, D. Dolfi, G. Lehoucq, A. Martin, G. Moille, L. Morvan, R. Braive, S. Combrié, and A. De Rossi, *APL Photonics* **4** (2019), 10.1063/1.5121774, arXiv:1901.05922.
- [33] R. Stockill, M. Forsch, G. Beaudoin, K. Pantzas, I. Sagnes, R. Braive, and S. Gröblacher, *Physical Review Letters* **123**, 163602 (2019), arXiv:1909.07850.

## Supplementary Material: High-Frequency GaAs Optomechanical Bullseye Resonator

N. C. Carvalho,<sup>1,\*</sup> R. Benevides,<sup>1</sup> M. Ménard,<sup>2</sup> G. S. Wiederhecker,<sup>1</sup> N. C. Frateschi,<sup>1</sup> and T. P. M. Alegre<sup>1,†</sup>

<sup>1</sup>Applied Physics Department and Photonics Research Center, University of Campinas, Campinas, SP, Brazil

<sup>2</sup>Department of Computer Science, Université du Québec à Montréal, Montréal, Canada

In order to determine the spatial distribution and polarization of the measured optical modes, we analyzed the group velocity dispersion of the optical spectra by investigating the frequency dependence of the Free Spectral Range (FSR). Adjacent longitudinal optical modes  $\omega_\mu$  in relation to a reference mode,  $\omega_0 (= 2\pi\nu_0)$ , and  $\mu (= m - m_0)$  can be expanded using the FSR as [1]:

$$\omega_\mu = \omega_0 + \mu D_1 + \frac{1}{2}\mu^2 D_2 + \frac{1}{6}\mu^3 D_3 + \dots, \quad (\text{S1})$$

where  $D_1/2\pi$  is the FSR and  $D_2/2\pi$  correspond to its variation rate with  $\mu$ , and so forth. Notice that in this case a positive  $D_2$  corresponds to anomalous group-velocity dispersion (GVD) for the  $\mu$ -mode.

In Fig. S1 (a) the measured optical spectrum of the 740 nm  $w_{\text{ring}}$  sample is provided. The optical mode at 193.3 THz is our used for measuring the mechanical breathing mode on our devices. This mode belongs to a family with a FSR of  $\sim 1.77$  THz, as displayed in Fig. S1 (b). To emphasize the anomalous dispersion nature for our mode we plot the residual dispersion,  $D_{\text{int}} = \omega_\mu - \omega_0 - \mu D_1$ , in Fig. S1 (c). By fitting Eq. S1 to the shifted frequency data shown in Fig. S1 (b) a  $D_2/(2\pi) = 20.6$  GHz is found.

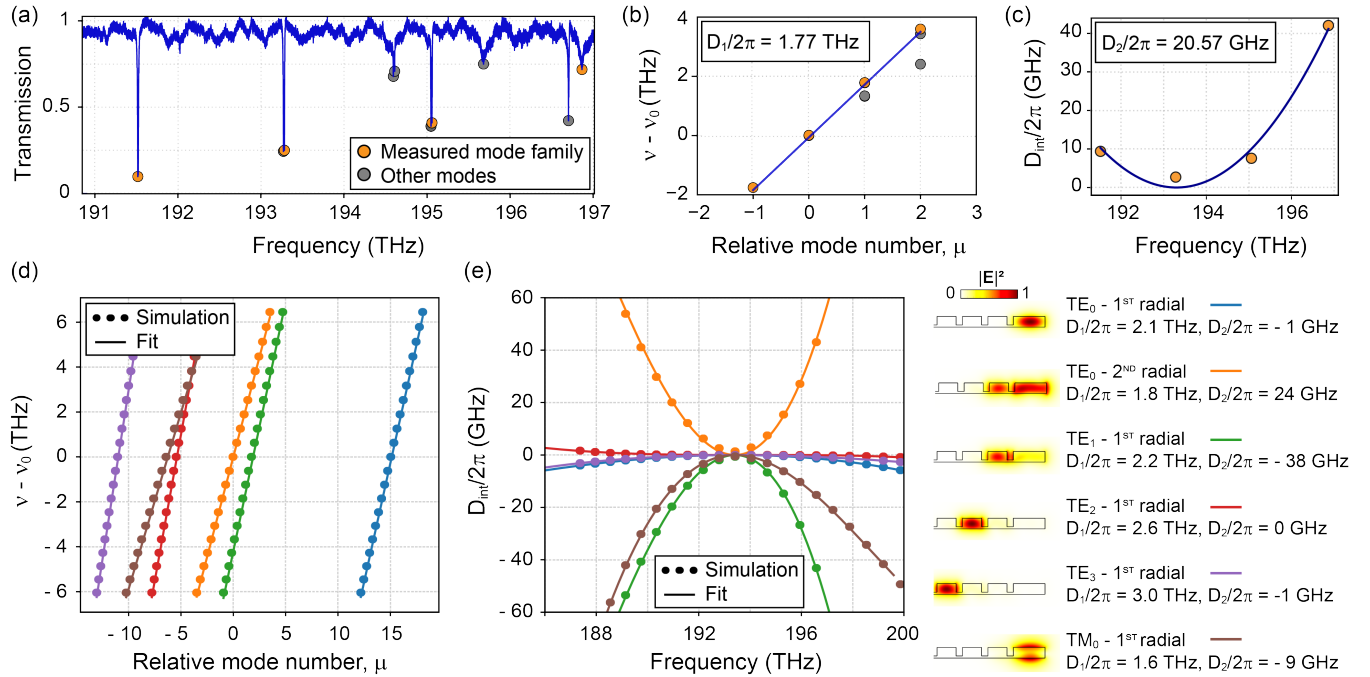


FIG. S1. (a) Optical spectrum of the 740 nm  $w_{\text{ring}}$  sample highlighting the measured mode family. (b) Linear fitting of the data points ( $\nu$  is the mode frequency and  $\nu_0 = 193.3$  THz). (c) Quadratic fitting of the residual dispersion ( $D_{\text{int}}$ ). FEM simulation of the linear (d) and quadratic (e) coefficients. Right: model results and respective simulated optical profiles.

In order to fully identify the optical mode, we used a Finite Element Method (FEM) to simulate the optical dispersion of the bullseye device that includes both geometrical and material dispersion [2]. The dimensions used in the simulation are  $R = 6\mu\text{m}$ ,  $w_{\text{ring}} = 746$  nm,  $a = 600$  nm, and  $w = 175$  nm and were recovered from the Scanning Electron Microscope image (SEM) show in Fig. 2 of the main text. The first outer groove,  $w_1$ , and the remaining device thickness,  $t$ , could not be precisely recovered from the SEM. They were therefore treated as free parameters – within the fabrication uncertainty – in order to match the simulated

\* natccar@ifi.unicamp.br

† alegre@unicamp.br

$D_1$  and  $D_2$  values to the measured ones. Figs S1 (d) and (e) show the FEM model results of our structure for the first six different mode families. The optical mode profile  $|E^2|$  and the fitting results for each mode family are also shown. Comparing this results with the experimental data, we have an unambiguous identification of the measured optical mode, which is a TE of second radial order. Notice that this mode have an avoided crossing with the mode in the first internal ring which explains its resulting anomalous dispersion. Finally, the same geometrical parameters and optical mode are used in the 3D anisotropic model to predict the optomechanical coupling rate,  $g_0$ , that agrees well with measured values.

- 
- [S1] L. Fujii, M. Inga, J. H. Soares, Y. A. V. Espinel, T. P. Mayer Alegre, and G. S. Wiederhecker, *Optics Letters* **45**, 3232 (2020), arXiv:2003.11625.  
[S2] A. H. Kachare, W. G. Spitzer, and J. E. Fredrickson, *Journal of Applied Physics* **47**, 4209 (1976).